Fast and quantitative noncontact laser ultrasound tapping detection of debonding in aerospace honeycomb sandwich panel based on Autoencoder-Softmax

Qiang Wu[a#], Weichen Xie[b#], Yi Xiong[c], Shiyuan Zhou[d*], Menglong Liu[b*], Zhongqing Su[e]

[a] Beijing Institute of Spacecraft Environment Engineering, China Academy of Space Technology, Beijing 100094, P.R. China

[b] School of Robotics and Advanced Manufacturing, Harbin Institute of Technology, Shenzhen 518055, P.R. China

[c] School of System Design and Intelligent Manufacturing, Southern University of Science and Technology, Shenzhen, 518055, P.R. China

[d] School of Mechanical Engineering, Beijing Institute of Technology, Beijing 100081, P.R. China

[e] Department of Mechanical Engineering, The Hong Kong Polytechnic University, Kowloon, Hong Kong Special Administrative Region, PR China

Abstract

Aerospace grade honeycomb sandwich panels (HSPs) feature ultra-thin skins and honeycomb walls and thus are prone to debonding defects during manufacturing and service. A fast, nondestructive, and noncontact laser ultrasound tapping method combining the local fine C-scan imaging and the global sparse C-scan is proposed to detect the debonding in the ultrathin aerospace HSP. Firstly, by measuring the thermoelastic laser-induced vibration signals with fine C-scan at a small-scale region including both known intact and debonding defects, an automatic labeling algorithm is proposed to construct the dataset for training the Autoencoder (AE)-Softmax model. Then, based on the trained AE-Softmax model, the sparse C-scan only at the centroid of each honeycomb cell can quickly identify suspicious defects with low credibility in the HSP. Further, the suspicious cells in HSP are fine scanned to differentiate the intact or debonding status according to the area proportion of the connected component in the C-scan image. Finally, experiments are carried out in a second HSP to validate the proposed method, that all the four diversified defects, including multiple debonding cells, one debonding wall, and adhesive removals, are successfully detected without false alarm, and the detection efficiency has been improved over 100 times compared with the conventional dense C-scan imaging.

Keywords: laser ultrasound, honeycomb sandwich panel, debonding, defect detection, machine learning

1. Introduction

Lightweight structures are important in spacecraft design to reduce vehicle weight, increase load levels and

# These authors contribute equally to the work.

* To whom correspondence should be addressed. Email: zhoushy@bit.edu.cn (Associate Prof. Shiyuan Zhou, *Ph.D.*) and liumenglong@hit.edu.cn. (Associate Prof. Menglong LIU, *Ph.D.*)

improve fuel efficiency [1]. Honeycomb sandwich panel (HSP) is a lightweight structure characterized by top and bottom skins bonded to a central honeycomb core through adhesive curing. This configuration offers high specific density, high specific stiffness and high specific strength [2,3], making it ideal for use in primary bearing structure, equipment platform and satellite fairing of space satellites [4–6]. A typical aerospace HSP features an aluminum skin of 0.3 mm thickness and a honeycomb core with a 0.04 mm thick honeycomb wall, with ventilation holes [7] and inserts [8] on the skin surface. However, during the manufacturing process and in service, HSPs are prone to suffer from interior defects that are not visible to the naked eye, such as debonding between the honeycomb core and the skin, inclusions [9] and liquid ingress [10] etc., resulting in their actual load levels being lower than the design load levels, which poses a threat to the structural safety of the entire vehicle. For detecting such debonding defects, traditional contact detection methods like ultrasonic C-scan are not feasible, as the coupling gel may enter the structure through ventilation holes and inserts, which poses a risk of resultant secondary damage [11]. This highlights the need for developing non-contact inspection techniques to ensure the integrity and safety of HSPs in aerospace applications.

Over the past few decades, a variety of non-contact inspection techniques have been explored for detecting defects in HSP. Among these techniques, both thermography [12] and shearography [13] are able to quickly image a large surface. However, when detecting debonding between the ultrathin honeycomb walls and the skin in HSP with thermography, it is necessary to coat the surface with a black paint to maximize the amount of absorbed heat if the sample surface has a high reflectivity [14]. The shearography usually adopts the thermally loading or vacuum loading, but it is not suitable for detecting debonding defect with large aspect ratio [15], which is exactly how debonding in the ultrathin HSP behaves. C-scan based air-coupled ultrasonic testing [16] and laser ultrasonic testing [17] allow for the detection of small-sized debonding defects with very small scan steps. However, due to the attenuation of ultrasonic waves during transmission, the air-coupled ultrasonic transmission technique is rarely applied to large thicknesses of HSPs as it results in poor signal-to-noise ratio (SNR) [18]. The C-scan based laser ultrasound pulse echo technique excites the normal propagating wave accompanying the surface ablation, which is destructive to the skin surface [19]. To avoid the surface ablation, an oil film constraint layer is usually coated on the surface [20], but in the case of aerospace HSP, the oil may leak into the interior and cause damage. In addition, achieving high resolution and SNR in detecting small-sized defects with conventional laser ultrasound indicates the lack of efficiency as it requires an extremely small scan step and extensive signal averaging [21,22]. Based on the non-contact laser-generated local vibration measured with the laser vibrometer, Blouin et al. [23] introduced a new technique called laser ultrasound tapping (LUT). LUT has the potential to sense local structural features around the scanned point and therefore does not require excessively small scan step

or large number of signal averaging. In the previous work, a novel reference-reconstruction algorithm based on LUT with a dense C-scan imaging was proposed for the quantitative detection of debonding honeycomb cells [24]. However, an in-depth investigation on the feature extraction to improve the detection accuracy and robustness in LUT is still missing. In addition, to achieve a reliable detection result, the detection efficiency must be compromised with a time-consuming dense scan with a small step. Hence, there still lacks an effective method that can realize a highly accurate, robust, fast, and nontact detection of debonding defect in HSP.

To enhance the efficiency and reliability of defect detection, various signal processing methods are employed, such as fast Fourier transform (FFT) [25], short-time Fourier transform [26], and wavelet transform [27] to extract features in time domain, frequency domain and time-frequency domain [28]. To downscale massive features extracted from the signals to few features, various machine learning algorithms have been used, such as principal component analysis (PCA) and autoencoder (AE). PCA is used to find valid features [29] in data or to downscale features [30]. Nonetheless, PCA has limitations in dealing with nonlinear relationships among variables [31] and struggles with complex data. Compared to PCA, AE excels at learning features in data [32] and has been combined with various classification models in the field of defect detection. For chatter detection, AE can be used for feature compression and defect detection through clustering algorithms [33]. Based on ultrasonic defect detection, the combination of AE and convolutional neural network (CNN) classifier improves the accuracy of CNN classification [34]. In addition, AE has also been used to detect faults in rotating machine [35], bearing [36] and electric motor [37], and has been proven to be superior to general algorithms.

In brief, various machine learning models have demonstrated the great progress in studies of classification. By integrating the machine learning with LUT-based detection techniques, a fast, accurate, robust, and quantitative noncontact detection of debonding defects in aerospace HSP is proposed in this study. By measuring the vibration signal at the honeycomb cell centroid, the sparse C-scan enables a fast and initial identification of intact and debonding regions with high credibility based on the trained AE-Softmax model. Then the remaining suspicious regions in HSP with low credibility is fine scanned to further differentiate the intact or debonding status according to the area of the connected domain. In addition to HSP, the proposed fast detection method can also be applied to the detection of internal defects in other periodical structures such as grid stiffened structure, lattice structure and corrugated structure.

The main contributions of this study are concluded as follows: (1) A fast detection method combining fine C-scan and sparse C-scan is proposed based on thermoelastic laser ultrasound tapping. In comparison to the conventional C-scan detection of aerospace-grade HSP, the proposed method shows a reduction of scanning points over 100 times. (2) A fine C-scan imaging algorithm is developed for locating the centroid of honeycomb

cells and detecting debonding honeycomb cells with detection sensitivity up to one debonding honeycomb wall. (3) A sparse C-scan detection method is constructed based on AE and Softmax, which achieves an initial fast detection by detecting only the centroid of each honeycomb cell.

The rest of the paper is organized as follows. Section 2 explains the sample, the experimental setup and the proposed detection method. Section 3 discusses the fine C scan imaging results and the performance of the AE-Softmax model, and validates the proposed fast scan detection method through experiments. Finally, the conclusion is drawn in Section 4.

2. Materials and methods

2.1. Specimen and experimental setup

As shown in **Fig. 1**a, an aerospace-grade aluminum HSP is investigated in this study, with a skin thickness and honeycomb wall thickness of only 0.3 mm and 0.04 mm, respectively. **Table 1** and **Table 2** show the material and geometric parameters of HSP, according to which two 500 mm × 500 mm HSPs are manufactured. As shown in **Fig. 1**b, two different debonding defects are prefabricated in HSP. The trimming wall features a trimmed honeycomb wall 2 mm shorter than the surrounding intact honeycomb walls. The adhesive removal is formed with the partial removal of the designated adhesive layer.

Specifically, as shown in **Fig. 2**, an Nd:YAG pulsed laser (Quantel Ultra) is used as a transient thermal actuator with a wavelength of 532 nm, a pulse duration of 9 ns, an energy of 8 mJ and a spot radius size of 2 mm. A two-wave mixing (TWM) laser vibrometer (Tecnar Discovery) is used as a detector with a wavelength of 1064 nm and a spot size of radius 0.2 mm. The incident angle of the Nd:YAG pulsed laser is approximately 53°, and the incident direction of the TWM laser vibrometer is perpendicular to the sample surface. The LUT signal is obtained by overlapping these two laser spots. The pulsed laser sends a rising edge signal to the data acquisition card (JYTEK PXIe-9817) to trigger the LUT signal acquisition. The HSP is mounted on a 2D motion stage and the scan path can be controlled through a PXI mainframe. The signal of 300 μs long is averaged 10 times with a sampling rate of 1 MHz. After removing the DC component, a Hanning window is applied to the signal, which is further zero padded to 1000 points corresponding to 1000 μs long. Then, with a finite impulse response low-pass filter featuring a passband frequency of 90 kHz and a stopband frequency of 200 kHz, the filtered amplitude spectrum is obtained by FFT.

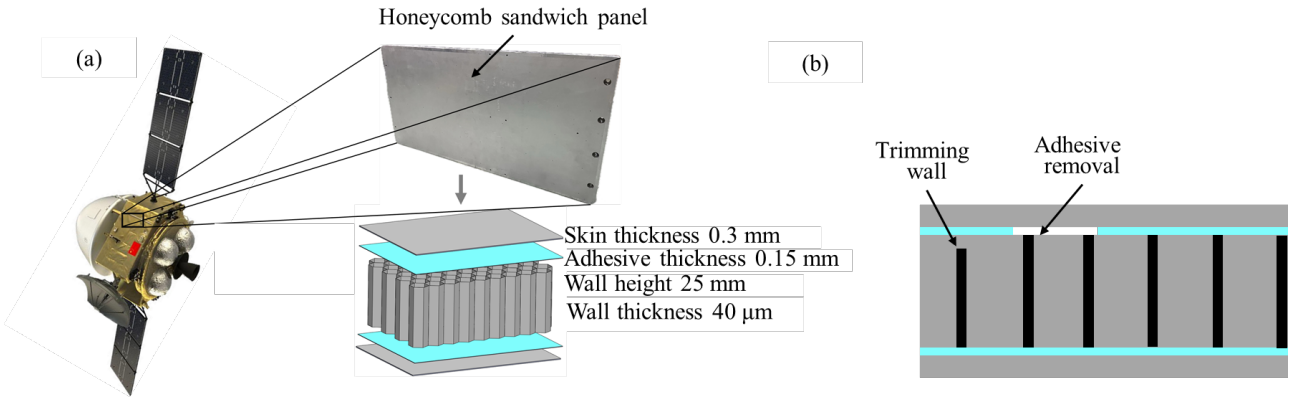

Fig. 1. (a) Schematic diagram of HSP sample and (b) schematic diagram of debonding defects.

Table 1 Material parameters of the HSP.

Part	Young's modulus E (GPa)	Density ρ (kg/m^3)	Poisson's ratio υ
Skin	70	2700	0.33
Adhesive layer	3	1673	0.3
Honeycomb core	70	2700	0.33

Table 2 Geometrical parameters of the honeycomb structure (units: mm).

Thickness of skin	Thickness of adhesive layer	Height of core	Length of core wall	Thickness of core wall
0.3	0.15	25	4	0.04

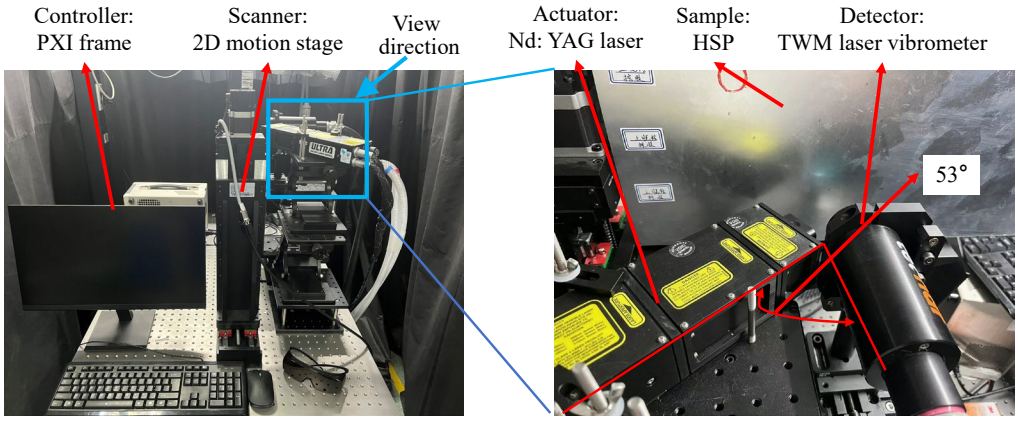

Fig. 2. Photo of LUT experiment.

2.2. Overview of detection method

The flowchart of the proposed fast scan LUT detection method is shown in **Fig. 3**, which mainly includes fine C-scan imaging and sparse C-scan at the honeycomb cell centroid. According to the experimental description in Section 2.1, the entire process includes the following key steps:

Step 1: Localization of one honeycomb cell centroid

A small area fine C-scan imaging is performed to locate the centroid of an intact honeycomb cell as the start point for the fast scan.

Step 2: Signal acquisition with a global sparse scan

The PXI mainframe controls the 2D motion stage to align the laser spots to the centroid of the cell. A sparse C-scan of only the honeycomb cell centroid is then executed. At the same time, the PXI mainframe reads the LUT signal acquired with the laser vibrometer.

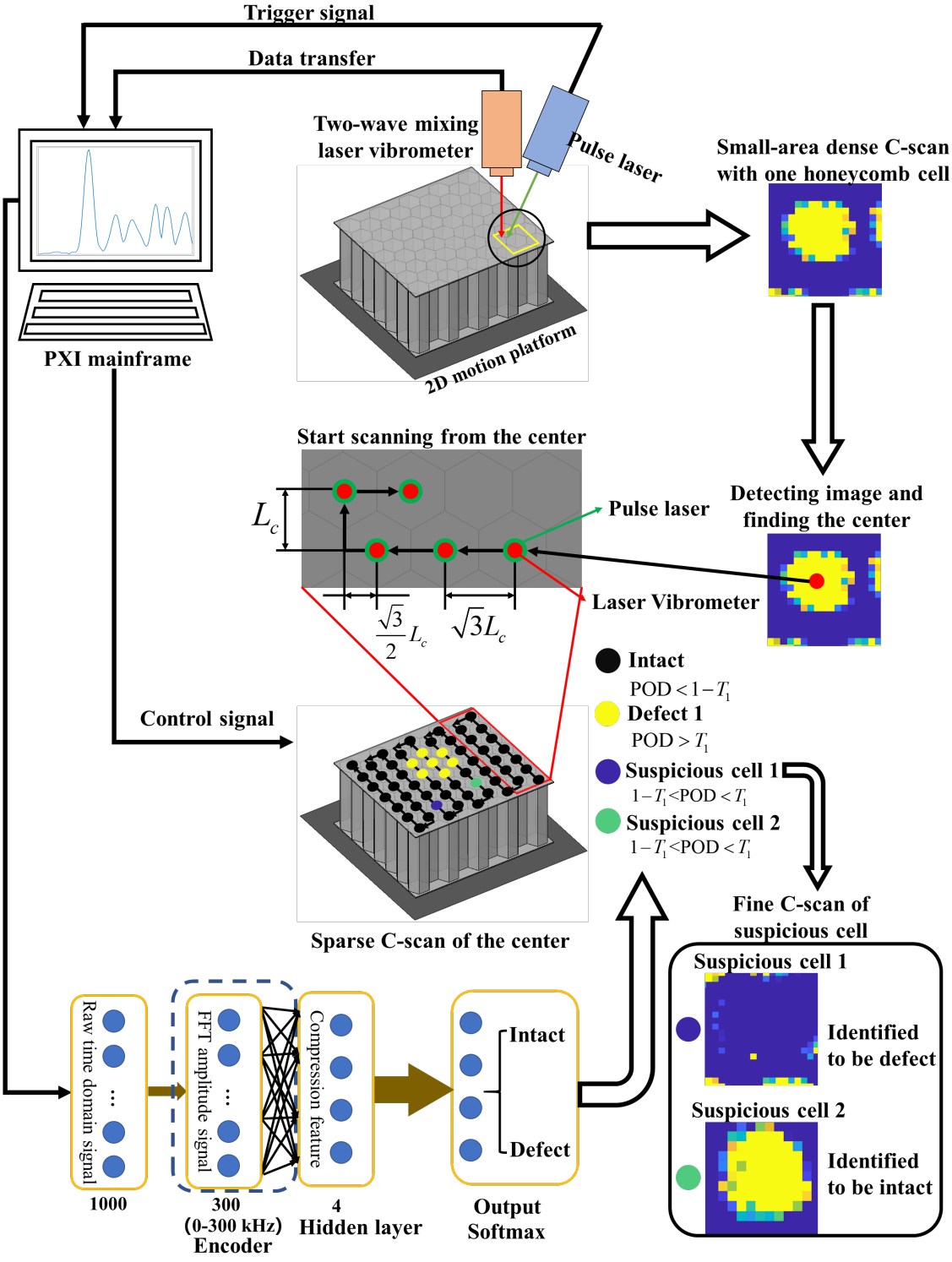

Fig. 3. Flowchart of fast LUT detection scan method.

Step 3: Classification of honeycomb cells based on the global sparse C-scan

Upon the signal processing as detailed in Section 2.1, the amplitude spectrum signal was input into the trained AE model. Then, four features of the hidden layer in the AE model are used as inputs to the trained Softmax classifier, which outputs the probability that the input belongs to a defect, as detailed in Section 2.4.

Step 4: Further detection of suspicious cell with local fine C-scan imaging

At the end of the sparse C-scan of the entire inspection region, a local fine C-scan of the regions with low detection credibility is performed, as detailed in Section 2.3. This approach prevents misclassification of the intact or debonding honeycomb cells. As shown in **Fig. 3**, honeycomb cells with a probability of defect (POD) less than $1-T_1$ (typically $T_1<50\%$, which can be adjusted) detected by sparse C-scan, as identified by a sparse C-scan, are considered to exhibit high intact cell credibility and are therefore judged to be intact. Honeycomb cell with a POD greater than T_1 is judged to be debonding cell, while honeycomb cell with a POD between T_1 and $1-T_1$ is judged to be suspicious cell. E.g., among these three possible defects, Defect 1 is identified as a debonding cell with a high defect credibility as $\mathrm{POD}>T_1$. The suspicious cells have PODs between T_1 and $1-T_1$, and are therefore deemed as suspicious cells, which need to be further detected with fine C-scan. Finally, the suspicious cells 1 and 2 are identified as defect and intact, respectively, and thus are prevented from misclassification.

2.3. Fine C-scan imaging

As shown in **Fig. 3**, the pulsed laser irradiates a specific area on the skin surface. When the power density of the pulsed laser is below the skin ablation threshold, a transient thermoelastic phenomenon occurs, leading to localized vibration at that spot. The change in vibration response resulting from the alteration of local stiffness around the debonding honeycomb cell can be used to characterize the debonding defect.

Fine C-scan imaging is realized based on frequency spectrum signal. As shown in **Fig. 4**, the debonding index I_d is calculated as:

$$I_d=\frac{A(f_1)}{\max[A(0):A(f_2)]}, \tag{1}$$

where $A(f_1)$ is the amplitude of the first-order natural frequency of the intact cell, and $\max[A(0):A(f_2)]$ is the maximum amplitude from 0 to f_2.

As shown in **Fig. 4**, it is evident that the debonding of the honeycomb wall near the centroid of the honeycomb cell leads to a decrease in the amplitude of its frequency spectrum at f_1, while an increase in the amplitude occurs at f_2. A typical C-scan imaging of 20×20 mm^2 with a step size of 0.5 mm based on Eq.(1), as illustrated in **Fig. 5**, shows the imaging difference between the debonding and intact honeycomb cells, in which the debonding cell disrupts the periodic honeycomb pattern.

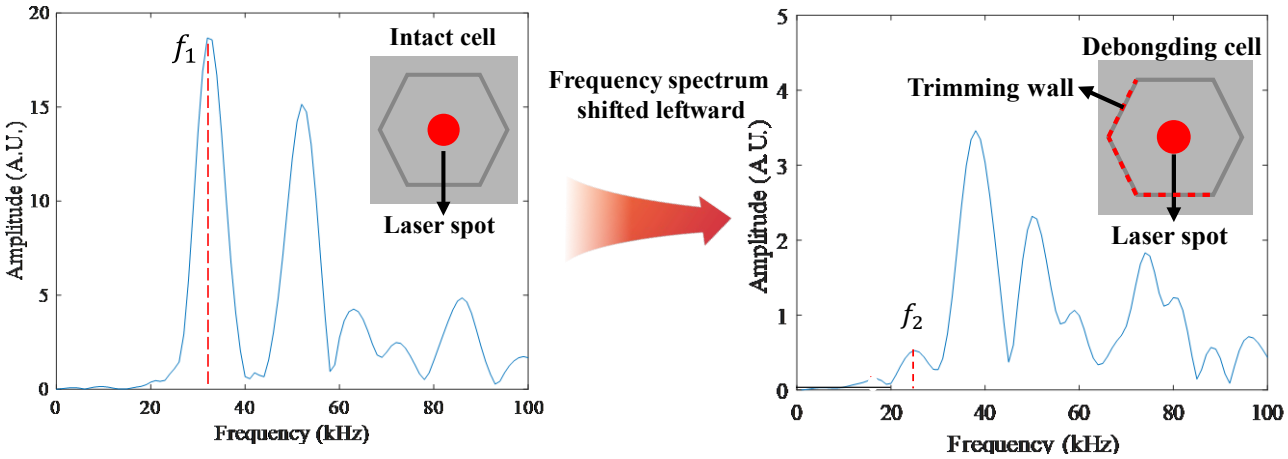

Fig. 4. The frequency spectrum of signal at the centroid of (a) intact cell and (b) debonding cell.

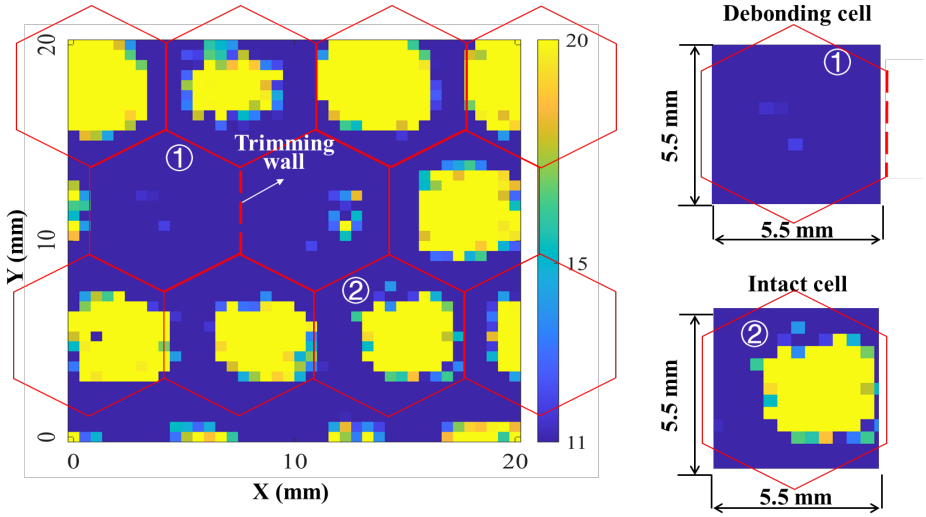

Fig. 5. Typical fine C-scan image containing only one honeycomb cell: (a) debonding cell and (b) intact cell.

In order to prevent misclassification of honeycomb cells via only the sparse C-scan, it is necessary to further conduct a fine C-scan imaging of the suspicious cells with a low credibility of sparse C-scan. The two fine C-scan images of 5.5 mm×5.5 mm corresponding to the debonding and intact cells are extracted from the typical C-scan imaging of 20 mm × 20 mm in **Fig. 5** for the illustration. A binarization process with a threshold of 11 is performed first. Then, based on the 8-neighborhood definition, the number of the connected component with a binarized value of one representing the honeycomb cell is calculated. The cell is determined to be intact when the number of pixels in the connected component is over 30 with a pixel size of 0.5 mm × 0.5 mm, covering 50% of a honeycomb cell. Otherwise, the cell is determined to be debonding.

2.4. AE-Softmax model-based debonding detection with fast C-scan

The AE-Softmax model training process is shown in **Fig. 6**, where the training set is firstly input into the AE model to obtain the compression features of the hidden layer, based on which the signal reconstruction is then carried out. The AE model is trained based on the unsupervised mode, the loss function is computed based on the raw signals and reconstructed signals, and the first fine tuning is performed by optimizing the parameters of the

autoencoder through the scaled conjugate gradient algorithm. The Softmax classifier is trained based on the supervised mode, and therefore requires inputs of the compression features and labels for all the samples. Using the features extracted by the autoencoder and the labels to which the features belong, the Softmax model is fine-tuned by minimizing the loss function through the scaled conjugate gradient algorithm.

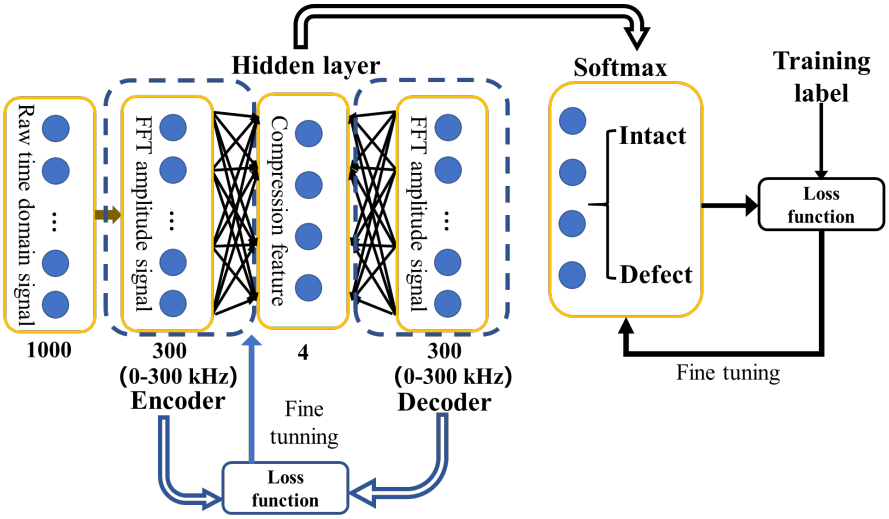

Fig. 6. Flowchart for AE-Softmax model training.

2.4.1 Automatic labeled dataset construction based on digital image processing

To acquire the dataset easily and accurately, and to prevent any artificial manipulation of the data, this study proposes an algorithm for automatic labeled dataset construction based on digital image processing techniques. The flowchart is illustrated in **Fig. 7**.

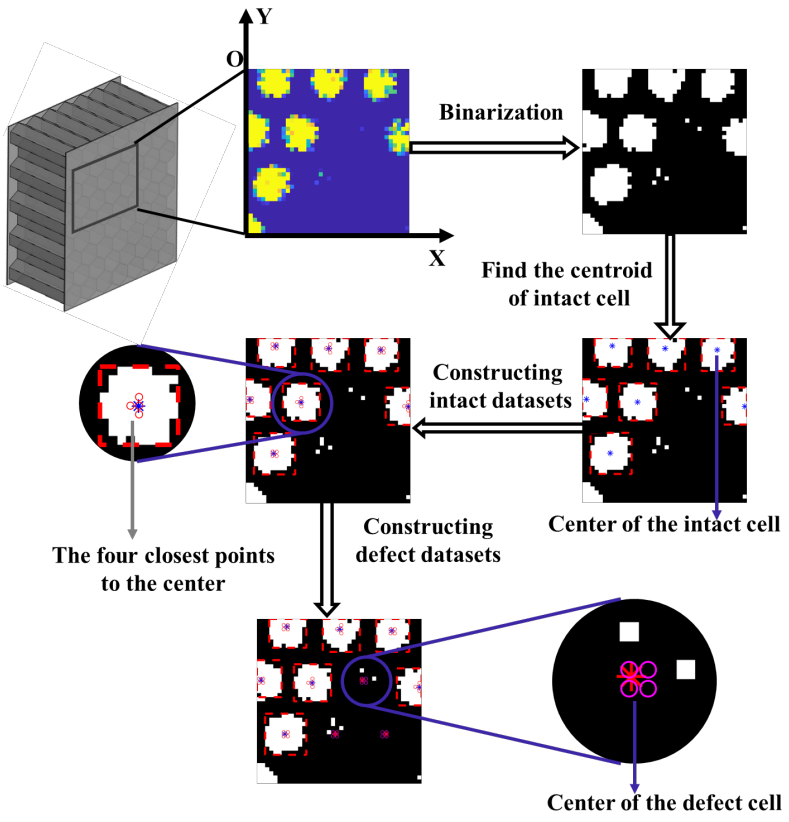

Fig. 7. Flowchart for construction of labeled dataset.

Step 1: Identification of intact honeycomb cell from fine C-scan image.

Initially, the C-scan image obtained through Eq. (1) is binarized with a threshold set to eleven. Next, all the connected components are identified using the two-pass algorithm [38] based on the 8-adjacency, defining the set $C=\{C_1,C_2,...,C_n\}$ that contains all the connected components. Subsequently, the connected components representing the intact cells, whose centroids are located within the C-scan image, are determined as:

$$\Omega(C)=\{C_i \mid C_i \in C, A(C_i)>A_N\} \bigcap \{C_j \mid C_j \in C, \frac{A(C_j)}{P(C_j)}>\alpha\}, \tag{2}$$

$$\alpha=\frac{\pi r^2}{2\pi r}=\frac{r}{2}, \tag{3}$$

where $\Omega(C)$ represents the connected components of the intact honeycomb cells in C, $A(C_i)$ and A_N indicate the number of the pixels in the connected component C_i and corresponding to the half area of the intact honeycomb cell, respectively. $P(C_j)$ denotes the perimeter of the connected component C_j. Approximating the shape of the honeycomb cell into a circle, α is calculated with Eq.(3) that represents the shape characteristics of the honeycomb cell. Based on the later C-scan image results, $r=3\,\text{mm}$ is taken.

Step 2: Construction of intact dataset.

The centroids of the connected components are selected as the centroids of the intact honeycomb cells. Owing to the scan step error of the motor or the manufacturing error of the HSP, the scanned point may not align exactly with the centroid of the honeycomb cell during the C-scan process. To ensure the dataset's accuracy, the following steps are taken. Initially, the four pixels closest to the centroids of each intact honeycomb cells in the C-scan image are determined based on the Euclidean distance. The Euclidean distance is calculated as follows:

$$d=\sqrt{(x-x_c^i)^2+(y-y_c^i)^2}, \tag{4}$$

where x and y represent the coordinates of the pixel points in the C-scan image, x_c^i and y_c^i denote the coordinates of the centroid of the i-th intact honeycomb cell in $\Omega(C)$, and d is the distance between the pixel and the centroid. The coordinates of the four pixels closest to the centroid (x_c^i,y_c^i) are found by Eq. (4), and their time-domain signals are stored as a dataset.

Step 3: Inference of defect cells and construction of defect dataset.

Firstly, choose an arbitrary centroid coordinate (x_0,y_0) obtained in Step 2. The approximated locations of the centroids of all the honeycomb cells in the C-scan image can be derived as:

$$H_d(P)=\{(P_{ix},P_{iy}) \mid P_{ix}=x_0+\sqrt{3}L_c n, P_{iy}=y_0+2L_c m, 0<P_{ix}<X_c, 0<P_{iy}<Y_c\}, \tag{5}$$

subject to $-\frac{X_c}{\sqrt{3}L_c} < n < \frac{X_c}{\sqrt{3}L_c}, -\frac{Y_c}{2L_c} < m < \frac{Y_c}{2L_c}, n \text{ and } m \in \text{Interger}$,

where H_d is the set of approximate coordinates of the centroid points of all honeycomb cells, (P_{ix}, P_{iy}) is the coordinate of the i-th honeycomb cell centroid, L_c is the length of the honeycomb wall, X_c and Y_c are the length of the C-scan image in the X and Y directions, respectively.

Define the set containing the centroids obtained in Step 2 as H_i, and calculate the Euclidean distance between the coordinates in H_d and the coordinates in H_i. If there exists a point $(P_{ix}, P_{iy}) \in H_d$ whose Euclidean distance between (P_{ix}, P_{iy}) and any point in H_i is less than L_c, then (P_{ix}, P_{iy}) is deemed as the centroid of the intact cell and thus removed from H_d. The remaining points in H_d represent the centroids of the defect honeycomb cells, and the defect dataset is obtained similarly following the procedure in Step 2.

2.4.2 Autoencoder model

AE is an unsupervised machine learning model comprising an encoder and a decoder. The encoder facilitates the conversion of high-dimensional inputs into low-dimensional features in the hidden layer, while the decoder reconstructs the low-dimensional features back to the original input dimensions. In this study, the AE model is used to extract key features from vibration signals in LUT experiments. To effectively capture these key features, the amplitude spectrum signals ranging from 0 to 300 kHz are employed as input for the AE model. Although the adopted FIR filter has a stopband frequency of 200 kHz, the amplitude response of the filter still has some energy between 200 kHz and 300 kHz, even though the signal has a lower amplitude in that band. Therefore, retaining the signal in the 200 kHz to 300 kHz range ensures that we do not lose potentially usable information. When $X \in \mathrm{R}^{b\times 1}$ and $\hat{X} \in \mathrm{R}^{b\times 1}$ are respectively used as input signals and reconstruction signals for the AE model (in this study $b = 300$), the AE model can be defined as:

$$a = f(X) = s(W_1 X + b_1), \tag{6}$$

$$\hat{X} = g(a) = s(W_2 a + b_2), \tag{7}$$

where a is the feature in the hidden layer, i.e., the low-dimensional features after compression by the AE model. X and $\hat{X}$ are the input signal and reconstructed signal, respectively. S is the transfer function between the encoder and the decoder, which, in this study, is the logistic sigmoid function. $W_1 \in \mathrm{R}^{m\times r}$ and $W_2 \in \mathrm{R}^{m\times r}$, $b_1 \in \mathrm{R}^{r\times 1}$ and $b_2 \in \mathrm{R}^{r\times 1}$ are the weight matrices and biases of the encoder and decoder, respectively, where

$r = 4$ is the hidden layer size [39,40].

The adopted loss function is the mean square error as:

$$\{W_1, W_2, b_1, b_2\} = \arg\min_{W_1, W_2, b_1, b_2} \frac{1}{m} \sum_{i=1}^{m} (X_i - \hat{X}_i)^2 , \tag{8}$$

where X_i and $\hat{X}_i$ represent the ith element of X and $\hat{X}$, respectively.

2.4.3 Softmax classifier

Softmax is trained in the supervised mode. To train the classifier, the features $a = \{a^1, a^2, ..., a^m\}$ and labels $t = \{t^1, t^2, ..., t^m\}$ of each sample are put into the Softmax classifier, which estimates the probability $p(t = j \mid a^i)$ for class $j = 1, 2, ...k$. The number of classes is $k = 2$, representing the intact and the debonding honeycomb cells respectively, and the sample is assigned to the class with the highest probability. The Softmax classifier is defined as [41]:

$$h_\theta(a^i) = \begin{bmatrix} p(t^i = 1 \mid a^i; \theta) \\ p(t^i = 2 \mid a^i; \theta) \end{bmatrix} = \frac{1}{\sum_{j=1}^{2} e^{\theta_j a^i}} \begin{bmatrix} e^{\theta_1^T a^i} \\ e^{\theta_2^T a^i} \end{bmatrix}, \tag{9}$$

where a^i is the feature vector of the ith sample, $p(t^i = 1 \mid a^i; \theta)$ and $p(t^i = 2 \mid a^i; \theta)$ are the probabilities that the ith sample is recognized as class 1 (intact) or class 2 (defect) by the classifier, and θ is the normalization parameter of the model ensuring that the sum of the probabilities equals one.

The loss function is the commonly used cross entropy function for classification problems, as follows:

$$J(\theta) = -\frac{1}{m} [\sum_{i=1}^{m} \sum_{j=1}^{k} 1\{t^i = j\} \log \frac{e^{\theta_j^T a^i}}{\sum_{l=1}^{k} e^{\theta_l^T a^i}}], \tag{10}$$

where $1\{t^i = j\}$ is an indicator function, if $t^i = j$ is true, $1\{t^i = j\} = 1$; otherwise, $1\{t^i = j\} = 0$.

3. Results and discussions

3.1. Fine C-scan imaging based on LUT detection technique

Fig. 8 illustrates the impact of different numbers of trimming walls at a cell on the frequency spectrum signal with LUT at the cell centroid. As shown in **Fig. 8**a, the amplitude of the time-domain signal diminishes progressively as the number of debonding honeycomb walls increases. The Fourier transform of the time-domain signal in **Fig. 8**a is used to obtain **Fig. 8**b, from which it demonstrates a gradual leftward shift in the spectrum with an increasing number of debonding honeycomb walls, indicated by a reduction in the amplitude at 33 kHz and a gradual increase in amplitude around 24 kHz. **Fig. 9** illustrates the impact of different size of adhesive

removal at a cell on the frequency spectrum signal with LUT at the cell centroid. The trend of a gradual leftward shift of the spectrum as the size of the adhesive removal becomes larger can also be seen in **Fig. 9**b. The reason is that as the debonding defects occur, the resulting loss of the local stiffness leads to the leftward shift of the frequency spectrum, which corroborates well with the conclusion made in the previous study [23]. Therefore, f_1 and f_2 in Eq.(1) are respectively taken as 32 kHz and 22 kHz.

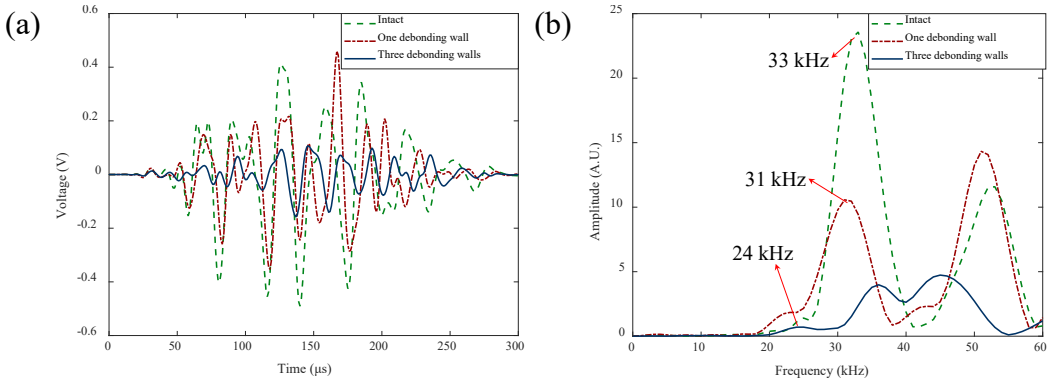

Fig. 8. Experimental LUT signal at the intact and trimming wall defect cell centroid: (a) time domain and (b) frequency domain.

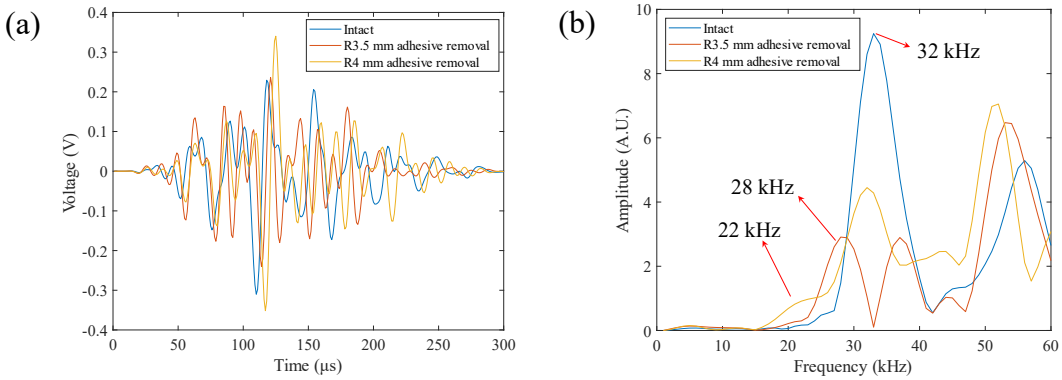

Fig. 9. Experimental LUT signal at the intact and adhesive removal defect cell centroid: (a) time domain and (b) frequency domain.

To acquire the dataset for training the AE-Softmax model, LUT C-scan experiments are initially conducted on several regions of HSP containing both intact and debonding cells. Subsequently, the signal processing procedure introduced in Section 2.1 and Eq.(1) are applied to the raw signal to extract the debonding index for C-scan imaging. The C-scan images in **Fig. 10** and **Fig. 11** display several typical trimming wall regions and adhesive removal regions. **Fig. 10**a-d indicate the number and location of honeycomb cells that may be affected by the trimming wall. However, it should be noted that the vibration response at the centroid will be affected once any of the surrounding six walls in the honeycomb cell is trimmed, as shown in **Fig. 10**d and h. The designed affected area of adhesive removal, as shown in **Fig. 11**a-d, may be larger than the actual affected honeycomb cells due to the flow of adhesive in the curing process. In summary, the capability of fine C-scan imaging to detect the debonding as small as an individual debonding honeycomb walls establishes the groundwork for the fast and quantitative debonding detection in HSP.

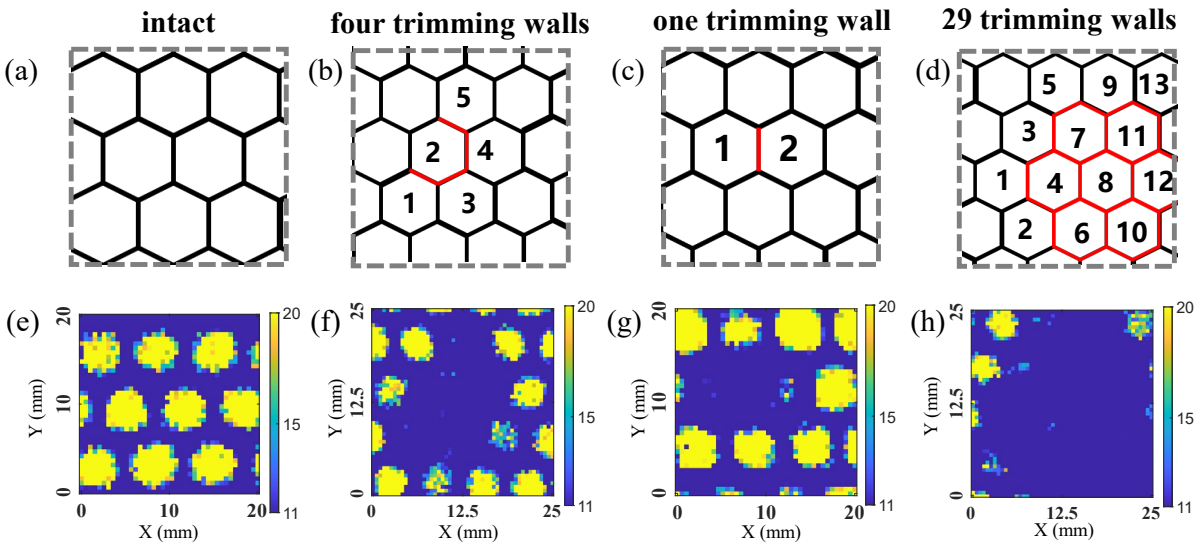

Fig. 10. (a-d) intact cells and cells with trimming wall debonding defects, and (e-h) corresponding C-scan imaging.

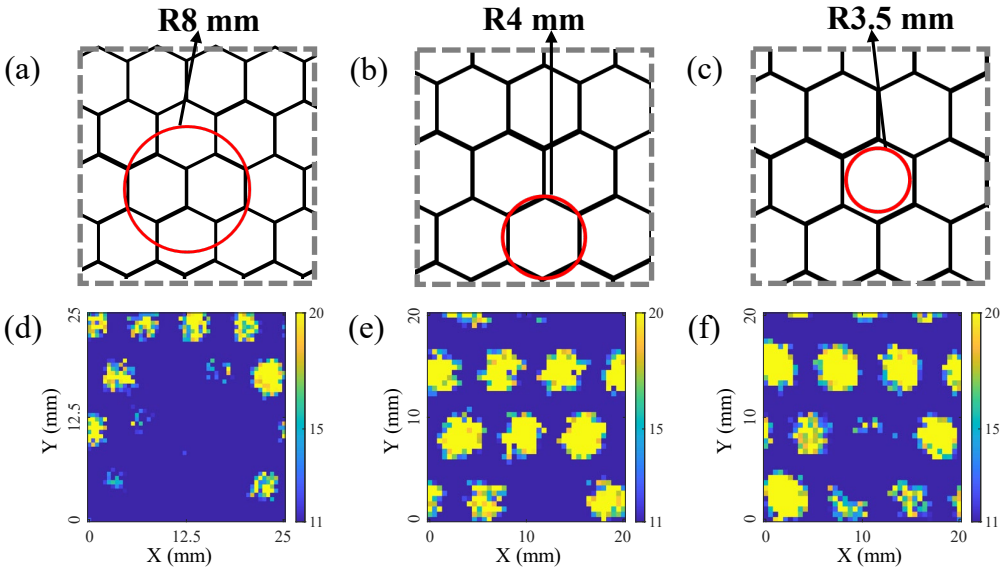

Fig. 11. The shape of adhesive removal (a-c) and fine C-scan imaging results (d-f) (units: mm).

3.2. AE-Softmax model training result

The dataset is constructed using the method described in Section 2.4, comprising a total of 1000 samples with an 8:2 ratio between intact and defect samples. Among 1000 samples, 850 are used for training and 150 for testing. Within the training set, the ratio of intact to defect samples is 14:3, while in the test set, it is 2:1. The AE model and the Softmax classifier training processes reach the convergence after 1500 and 59 epochs, respectively. **Fig. 12** shows the training performance of the autoencoder. At the epoch number 2000, the loss calculated with Eq. (8) is approximately 2.92. In this study, accuracy, sensitivity and specificity are mainly used to evaluate model performance.

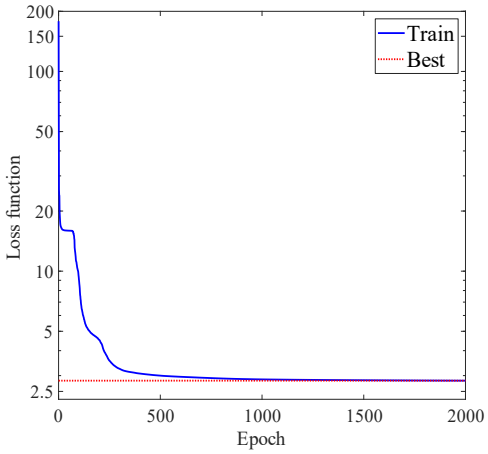

Fig. 12. The training history of the autoencoder

The accuracy of the AE-Softmax model, representing the proportion of correctly classified samples to the total samples, is defined by the following equation:

$$Acc = \frac{\mathrm{TP} + \mathrm{TN}}{\mathrm{TP} + \mathrm{FP} + \mathrm{FN} + \mathrm{TN}}, \tag{11}$$

where TP (true positive) represents the actual intact type predicted as intact, FN (false negative) represents the actual intact type predicted as defect, TN (true negative) represents the actual defect type predicted as defect and FP (false positive) presents the actual defect type predicted as intact.

Similarly, the sensitivity and the specificity are defined by the following respective equations:

$$Sen = \frac{\mathrm{TP}}{\mathrm{TP+FN}}. \tag{12}$$

$$Spe = \frac{\mathrm{TN}}{\mathrm{TN+FP}}. \tag{13}$$

The Softmax classifier outputs the probabilities $p(t^i = 1 \mid a^i; \theta)$ and $p(t^i = 2 \mid a^i; \theta)$, which determine the detection results by comparing with a threshold, which is usually 50%. For example, a value of $p(t^i = 1 \mid a^i; \theta) < 50\%$ (a.k.a. $p(t^i = 2 \mid a^i; \theta) > 50\%$) is identified as defect. The prediction results based on the test set are shown in **Table 3**, indicating that the sparse C-scan machine learning model proposed in this study has excellent performance in detecting debonding defects in HSP.

Table 3 AE-Softmax model test result.

Indicator	Accuracy	Sensitivity	Specificity
Value	98%	100%	94%

3.3. Results with combined sparse-fine LUT C-scan

The trained AE-Softmax model has been utilized for experimental validation of the proposed method using a second HSP with identical geometrical and material parameters. **Fig. 13** illustrates a sparse scan detection process complemented with several local fine scan imaging conducted in the region of the HSP, and the resulted

PODs with the trained AE-Softmax model in several typical regions are listed in **Table 4**. All the PODs corresponding to Defects 1 and 4 are over 80%, while those at Defects 2 and 3 are between 70% and 80%. In addition, only two intact cells named as Intactness 1 and 2 show PODs over 20%. Hence, supposing the defect threshold T_1 set to 80%, Defects 2 and 3, together with Intactness 1 and 2, are deemed as the suspicious cells as a result of $1-T_1<\mathrm{POD}<T_1$. Hence a fine C-scan imaging of 5.5 mm × 5.5 mm centered on the four suspicious cells centroid are performed to avoid the misclassification. The connectivity analysis based on the fine C-scan imaging as explained in Section 2.3 is performed to correctly identify the four suspicious cells, demonstrating the effectiveness of the proposed method.

It is also worth noting that since Defects 2 and 3 are adhesive removal defects, the actual defects are smaller than the prefabricated defects due to the flow of the adhesive layer of the HSP during the preparation process. In addition, by lowering T_1, the number of scan points can be reduced, thus improving the detection efficiency. For example, when $T_1=70\%$, only the suspicious cells with POD between 30% and 70% need to be subjected to fine C-scan. In this case, it is only necessary to detect Intactness 2 with a POD in that range.

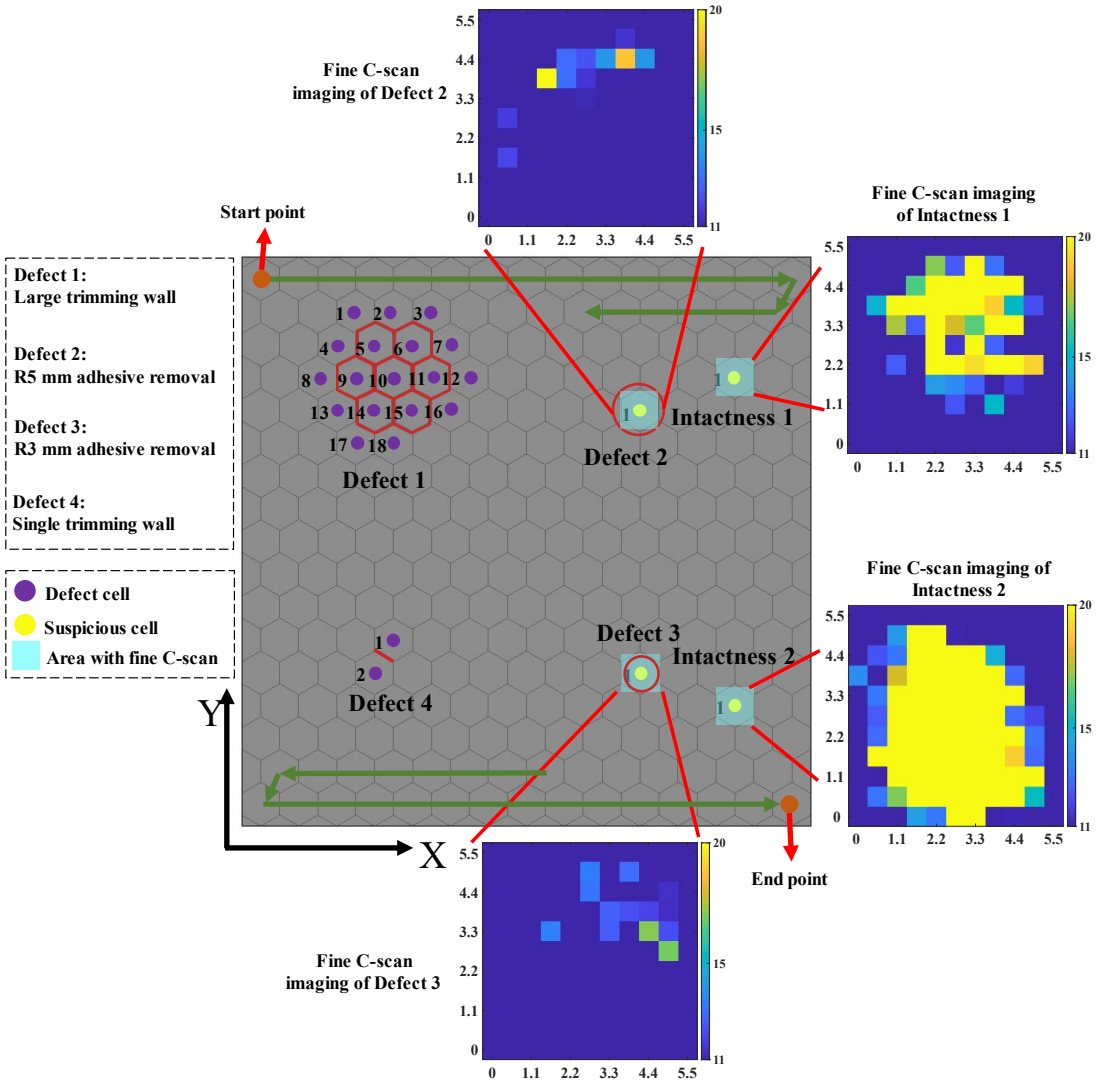

Fig. 13. Schematic diagram of debonding defect and fast scan detection (unit: mm).

Table 4 AE-Softmax model prediction probability of defect.

ID	POD	ID	POD	ID	POD
Defect 1-1	86.73%	Defect 1-2	92.51%	Defect 1-3	93.11%
Defect 1-4	90.18%	Defect 1-5	94.23%	Defect 1-6	94.25%
Defect 1-7	96.62%	Defect 1-8	96.44%	Defect 1-9	94.81%
Defect 1-10	98.06%	Defect 1-11	85.50%	Defect 1-12	88.74%
Defect 1-13	93.23%	Defect 1-14	89.96%	Defect 1-15	86.04%
Defect 1-16	90.15%	Defect 1-17	90.51%	Defect 1-18	83.31%
Defect 2	71.40%	Defect 3	71.43%	Defect 4-1	98.57%
Defect 4-2	90.57%	Intact 1	24.05%	Intact 2	31.20%

3.4. Comparison between noncontact LUT and contact ultrasound detection

In order to verify the reliability of the test results, the areas with four defects in the HSP samples are further examined with the contact ultrasound C-scan. The detection device is shown in **Fig. 14**, that a 128 ×128 elements transducer at a center frequency of 10 MHz is connected to the multi-channel pulse exciter and receiver platform Dolphicam. The transducer is fully coupled to the detection areas in the HSP with sprinkled water. The ultrasound imaging based on the signals within the time gate corresponding to the back wall echo of the skin is shown in **Fig. 15**. For the imaging of Defects 1 and 4 made of trimming walls, as shown in **Fig. 15** a and d, the extremely small thickness of the honeycomb wall results in negligible wave reflection from the trimming walls, which makes Defect 4 with a single trimming wall defect unnoticeable from the ultrasound C-scan imaging. By contrast, as the adhesive removal for area-based debonding Defects 2 and 3 significantly influences the wave reflection, the contact ultrasound detection technique can obtain reliable C-scan imaging results of debonding, as shown in **Fig. 15**b and c.

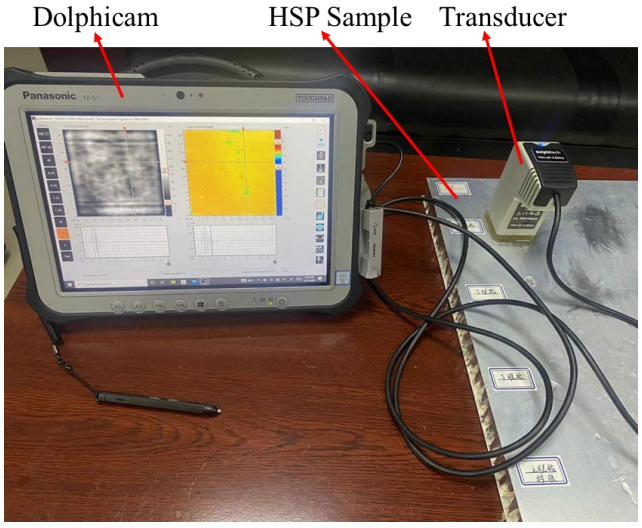

Fig. 14. Contact ultrasonic C-scan inspection equipment.

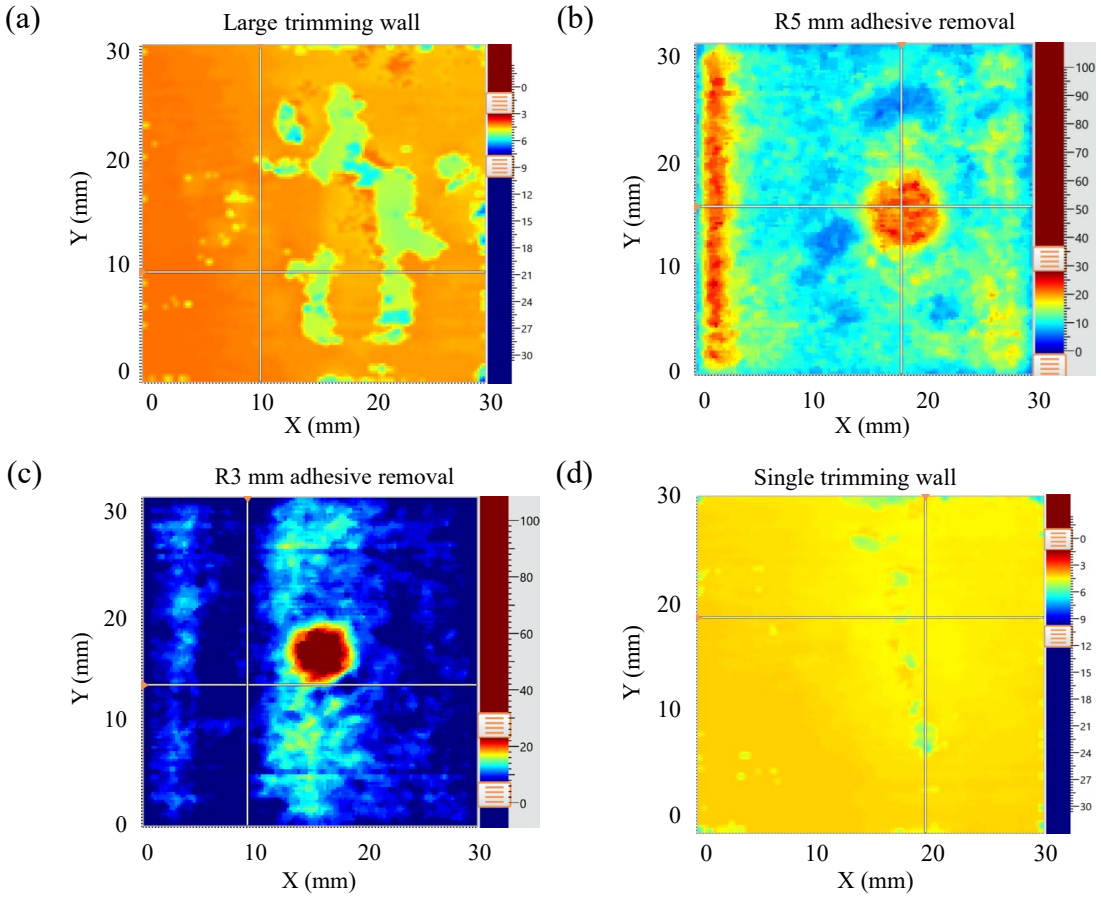

Fig. 15. Contact ultrasound C-scan test results for Defect (a) 1, (b) 2, (c) 3, and (d) 4 (illustrate in **Fig. 13**).

To illustrate the sensitivity of the proposed LUT method in detecting HSP, a 20 mm × 20 mm fine C-scan imaging is performed in Defects 1 and 4, respectively. As shown in **Fig. 16**a, the periodic regular honeycomb pattern disappears in the C-scan image due to the presence of a large number of debonding cells at Defect 1. Similarly, as two debonding cells are affected by the shared single debonding honeycomb wall at Defect 4, two honeycomb cell patterns are disappeared in **Fig. 16**b.

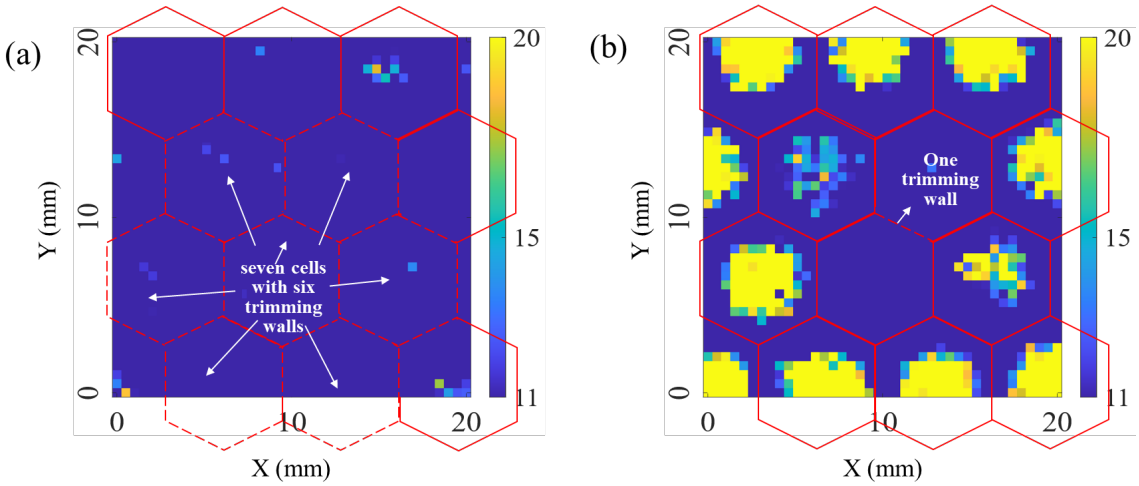

Fig. 16. Fine C-scan imaging of (a) Defect 1 and (b) Defect 4.

In addition, compared to the conventional fine C-scan detection, the proposed hybrid sparse and fine LUT scan method provides a significant decrease in the number of detection points. If the area to be detected has C_x

cells in the X-direction and C_y in the Y-direction, the improvement in detection efficiency can be estimated by the number of scan points.

$$EI = \frac{P_x \times P_y}{C_x \times C_y + P_{\text{fine\_cell}} \eta (C_x \times C_y)} \tag{14}$$

where EI is the efficiency improvement index, P_x and P_y represent the point counts required for conventional C-scans in the X and Y directions, respectively. $P_{\text{fine\_cell}}$ signifies the number of points for a 5.5 mm × 5.5 mm fine C-scan aimed at preventing misclassification and η represents the proportion of honeycomb cells requiring fine C-scan to the total cells. For the sample in this study, $P_x = 2\sqrt{3}L_c C_x$ $(13.86C_x)$, $P_y = 3L_c C_y$ $(12C_y)$, $P_{\text{fine\_cell}} = 121$ under the step of 0.5 mm, which provides the relationship between the threshold T_1 and EI as listed in **Table 5**. Even with a high threshold T_1 of 80%, the efficiency improvement can reach 58 times, which further improves to around 171 times when T_1 decreases to 60%.

Table 5 The variation of defect probability threshold in fine C-scan and efficiency.

Defect threshold T_1	80%	70%	60%
Scan points of proposed method	731	610	247
Efficiency improvement	58.02	69.53	171.71

Compared with the traditional detection methods, the proposed fast detection method combining laser ultrasound tapping and AE-Softmax model significantly improves the noncontact detection efficiency without damaging the test samples. In addition, as the room temperature and pressure do not exert a significant influence on the dynamic characteristics of the HSP, the detection results are hardly influenced by both factors. Hence, it is convinced that the proposed LUT method combining fast sparse scan and fine C-scan imaging has a strong robustness against the variation of the room temperature and pressure.

4. Conclusion

Combining the global sparse and local fine scan, this study proposes an efficient LUT noncontact detection method of debonding in the aerospace ultrathin aluminum HSP. To facilitate the training of the AE-Softmax model, this study proposes a method of local fine C-scan for the automatic construction of datasets and labels using digital image processing techniques. The data of sparse C-scan at the cell centroid is then input into the trained AE-Softmax model to identify the bonding status. Finally, the identified suspicious HSP cells go through a further fine C-scan to improve the detection effectiveness. Based on the test set, this study demonstrated the effectiveness

of the proposed AE-Softmax model in detecting debonding defects in HSP in terms of the accuracy, sensitivity and specificity. Compared to the presented contact ultrasound C-scan, the proposed fast detection method is free from the contact with the sample, and can have higher sensitivity to the trimming wall-type debonding defects. In addition, an improvement of detection efficiency up to 171 times with defect threshold T_1 of 60% compared to the conventional dense C-scan imaging is achieved. Hence, the proposed noncontact method shows its great potential in debonding detection in aerospace HSP with a high accuracy and efficiency. The experimental approach in this study is based on moving the HSP sample and fixing the detection equipment to achieve the LUT. However, in the engineering application, it is necessary to fix the sample and move the detection equipment to improve the detection efficiency. In addition, samples may have stains on the surface, which may degrade the laser tapping and the acquisition of the vibration signals in the proposed LUT method. Future work will focus on the integration of detection and excitation lasers to realize the detection of HSP by keeping the HSP sample still, and the increase of repetition frequency of the excitation laser to further improve the detection efficiency.

Authorship contribution

Qiang Wu: Conceptualization, Writing – original draft. **Weichen Xie:** Data curation, Investigation, Methodology, Writing – original draft. **Yi Xiong:** Validation, Visualization. **Shiyuan Zhou:** Methodology. **Menglong Liu:** Funding acquisition, Supervision, Writing - review & editing. **Zhongqing Su:** Visualization.

Declaration of conflicting interests

The authors declare that they have no known competing financial interests or personal relationships that could have appeared to influence the work reported in this paper.

Acknowledgements

The authors would like to thank the support from the National Science and Technology Major Project (Project No. 2022ZD0117302), National Natural Science Foundation of China (Grant No. 52475153), Basic and Applied Basic Research Foundation of Guangdong Province (Grant No. 2023A1515011032), Shenzhen Stable Support Grant (Grant No. 20231130153036001).

Data availability

Data will be made available on request.

References

[1] W.Z. Jiang, X.C. Teng, X.H. Ni, X.G. Zhang, X. Cheng, W. Jiang, D. Han, Y. Zhang, X. Ren, An improved re-entrant honeycomb with programmable densification and multistage energy-absorbing performance, Eng. Struct. 301 (2024) 117318. https://doi.org/10.1016/j.engstruct.2023.117318.

[2] X.Y. Wei, J. Xiong, J. Wang, W. Xu, New advances in fiber-reinforced composite honeycomb materials, Sci. China Technol. Sci. 63 (2020) 1348–1370. https://doi.org/10.1007/s11431-020-1650-9.

[3] M. Liu, W. Zhang, X. Chen, L. Li, K. Wang, H. Wang, F. Cui, Z. Su, Modelling guided waves in acoustoelastic and complex waveguides: From SAFE theory to an open-source tool, Ultrasonics 136 (2024) 107144. https://doi.org/10.1016/j.ultras.2023.107144.

[4] A. Boudjemai, A. Mankour, H. Salem, R. Amri, R. Hocine, B. Chouchaoui, Inserts thermal coupling analysis in hexagonal honeycomb plates used for satellite structural design, Appl. Therm. Eng. 67 (2014) 352–361. https://doi.org/10.1016/j.applthermaleng.2014.03.060.

[5] A. Aborehab, M. Kassem, A. Farid Nemnem, M. Kamel, H. Kamel, Configuration design and modeling of an efficient small satellite structure, Eng. Solid Mech. 8 (2020) 7–20. https://doi.org/10.5267/j.esm.2019.9.002.

[6] G. Bianchi, G.S. Aglietti, G. Richardson, Development of efficient and cost-effective spacecraft structures based on honeycomb panel assemblies, IEEE Aerosp. Conf. Proc. (2010) 1–10. https://doi.org/10.1109/AERO.2010.5446748.

[7] V.K. Goyal, S. Maghsoudy-Louyeh, Proof test methodology for reducing the risk of unvented honeycomb core failures in aerospace structures, J. Sandw. Struct. Mater. 25 (2023) 61–76. https://doi.org/10.1177/10996362221116887.

[8] D. Zenkert, The Handbook of Sandwich Construction, Dan Zenkert, Ed. Nord. Ind. Fund (NI), Oslo, Norway, Swedish Natl. Board Ind. Tech. Dev. (NUTEK), Stock. Sweden. (1997) 442.

[9] P. Wang, L. Zhou, G. Liu, Y. Pei, In situ near-field microwave characterization and quantitative evaluation of phase change inclusion in honeycomb composites, NDT and E Int. 121 (2021) 102469. https://doi.org/10.1016/j.ndteint.2021.102469.

[10] P. Wang, Y. Pei, L. Zhou, Near-field microwave identification and quantitative evaluation of liquid ingress in honeycomb sandwich structures, NDT and E Int. 83 (2016) 32–37. https://doi.org/10.1016/j.ndteint.2016.06.002.

[11] S. Sikdar, J. Pal, Bag of visual words based machine learning framework for disbond characterisation in composite sandwich structures using guided waves, Smart Mater. Struct. 30 (2021). https://doi.org/10.1088/1361-665X/ac01a8.

[12] R. Souri-Solut, M. Farahani, P. Meshkizadeh, S. Asghari, Investigating the Excellence of Different Thermography Approaches to Subsurface Dis-bonds Detection in Aluminum Honeycomb Sandwich Structures, J. Nondestruct. Eval. 42 (2023) 1–20. https://doi.org/10.1007/s10921-023-01006-z.

[13] X. Liu, L. Zhu, P. Yan, B. Wang, Y. Wang, Quasi-real dataset generation and network improvement in defect detection based on shearography, Opt. Laser Technol. 171 (2024) 110392. https://doi.org/10.1016/j.optlastec.2023.110392.

[14] T. Rellinger, P.R. Underhill, T.W. Krause, D. Wowk, Combining eddy current, thermography and laser scanning to characterize low-velocity impact damage in aerospace composite sandwich panels, NDT and E Int. 120 (2021) 102421. https://doi.org/10.1016/j.ndteint.2021.102421.

[15] B. Guo, X. Zheng, M. Gerini-Romagnoli, L. Yang, Digital shearography for NDT: Determination and demonstration of the size and the depth of the smallest detectable defect, NDT and E Int. 139 (2023) 102927. https://doi.org/10.1016/j.ndteint.2023.102927.

[16] Z. Zhou, B. Ma, J. Jiang, G. Yu, K. Liu, D. Zhang, W. Liu, Application of wavelet filtering and Barker-coded pulse compression hybrid method to air-coupled ultrasonic testing, Nondestruct. Test. Eval. 29 (2014) 297–314. https://doi.org/10.1080/10589759.2014.941840.

[17] M.T. Thai, H. Ahmed, S.C. Hong, J.R. Lee, J.B. Ihn, Broadband Laser Ultrasonic Excitation and Multi-band Sensing for Hierarchical Automatic Damage Visualization, Int. J. Aeronaut. Sp. Sci. 20 (2019) 913–932. https://doi.org/10.1007/s42405-019-00210-4.

[18] H. Li, Z. Zhou, Detection and characterization of debonding defects in Aeronautical honeycomb sandwich composites using noncontact air-coupled ultrasonic testing technique, Appl. Sci. 9 (2019). https://doi.org/10.3390/app9020283.

[19] D.A. Hutchins, R.J. Dewhurst, S.B. Palmer, Directivity patterns of laser-generated ultrasound in aluminum, J. Acoust. Soc. Am. 70 (1981) 1362–1369. https://doi.org/10.1121/1.387126.

[20] X. Kou, C. Pei, T. Liu, S. Wu, T. Liu, Z. Chen, Noncontact testing and imaging of internal defects with a new Laser-ultrasonic SAFT method, Appl. Acoust. 178 (2021) 107956. https://doi.org/10.1016/j.apacoust.2021.107956.

[21] K. Zhang, S. Li, Z. Zhou, Quantitative analysis of voids in multi-layer bonded structures based on transmitted laser ultrasonic waves, Arch. Civ. Mech. Eng. 19 (2019) 79–90. https://doi.org/10.1016/j.acme.2018.08.004.

[22] J.R. Lee, S.Y. Chong, N. Sunuwar, C.Y. Park, Repeat scanning technology for laser ultrasonic propagation imaging, Meas. Sci. Technol. 24 (2013). https://doi.org/10.1088/0957-0233/24/8/085201.

[23] A. Blouin, C. Néron, B. Campagne, J.P. Monchalin, Applications of laser tapping and laser ultrasonics to aerospace composite structures, Insight Non-Destructive Test. Cond. Monit. 52 (2010) 130–133. https://doi.org/10.1784/insi.2010.52.3.130.

[24] W. Xie, T. Wang, S. Zhou, Q. Wu, M. Liu, Quantitative reconstruction of debonding in ultra-thin honeycomb sandwich panel based on noncontact thermoelastic laser tapping, Measurement 242 (2025) 116160. https://doi.org/10.1016/j.measurement.2024.116160.

[25] X. Li, E.A. Patterson, W.C. Wang, W.J.R. Christian, Prediction of Residual Strains Due to In-Plane Fibre Waviness in Defective Carbon-Fibre Reinforced Polymers Using Ultrasound Data, J. Nondestruct. Eval. 42 (2023) 1–15. https://doi.org/10.1007/s10921-022-00910-0.

[26] H. Mohammad, F. Vlasic, B. Maya, M.A. Shehadeh, P. Mazal, New evaluation method for defects propagation in toroidal roller bearings using dominant frequency of acoustic emission, Nondestruct. Test. Eval. 00 (2024) 1–25. https://doi.org/10.1080/10589759.2024.2402885.

[27] V. Rajendran, A. Prathuru, C. Fernandez, N. Faisal, Acoustic emission wave propagation in pipeline sections and analysis of the effect of coating and sensor location, Nondestruct. Test. Eval. 00 (2024) 1–31. https://doi.org/10.1080/10589759.2024.2390996.

[28] B. Debnath, R. Kumar, A new Tapered-L shaped springs based MEMS piezoelectric vibration energy harvester designed for small rolling bearing fault detection, Microsyst. Technol. 26 (2020) 2407–2422. https://doi.org/10.1007/s00542-020-04783-z.

[29] M.P. Uddin, M. Al Mamun, M.I. Afjal, M.A. Hossain, Information-theoretic feature selection with segmentation-based folded principal component analysis (PCA) for hyperspectral image classification, Int. J. Remote Sens. 42 (2021) 286–321. https://doi.org/10.1080/01431161.2020.1807650.

[30] T.R. Gadekallu, N. Khare, S. Bhattacharya, S. Singh, P.K.R. Maddikunta, I.H. Ra, M. Alazab, Early detection of diabetic retinopathy using pca-firefly based deep learning model, Electron. 9 (2020) 1–16. https://doi.org/10.3390/electronics9020274.

[31] E.C. Malthouse, Limitations of nonlinear PCA as performed with generic neural networks, IEEE Trans. Neural Networks 9 (1998) 165–173. https://doi.org/10.1109/72.655038.

[32] Z. Zhang, T. Jiang, S. Li, Y. Yang, Automated feature learning for nonlinear process monitoring – An approach using stacked denoising autoencoder and k-nearest neighbor rule, J. Process Control 64 (2018) 49–61. https://doi.org/10.1016/j.jprocont.2018.02.004.

[33] B. Liu, C. Liu, Y. Zhou, D. Wang, Y. Dun, An unsupervised chatter detection method based on AE and merging GMM and K-means, Mech. Syst. Sig. Process. 186 (2023) 109861.

https://doi.org/10.1016/j.ymssp.2022.109861.

[34] N. Munir, J. Park, H.J. Kim, S.J. Song, S.S. Kang, Performance enhancement of convolutional neural network for ultrasonic flaw classification by adopting autoencoder, NDT and E Int. 111 (2020) 102218. https://doi.org/10.1016/j.ndteint.2020.102218.

[35] J. Wu, Z. Zhao, C. Sun, R. Yan, X. Chen, Fault-Attention Generative Probabilistic Adversarial Autoencoder for Machine Anomaly Detection, IEEE Trans. Ind. Informatics 16 (2020) 7479–7488. https://doi.org/10.1109/TII.2020.2976752.

[36] X. Huang, G. Wen, S. Dong, H. Zhou, Z. Lei, Z. Zhang, X. Chen, Memory Residual Regression Autoencoder for Bearing Fault Detection, IEEE Trans. Instrum. Meas. 70 (2021). https://doi.org/10.1109/TIM.2021.3072131.

[37] E. Principi, D. Rossetti, S. Squartini, F. Piazza, Unsupervised electric motor fault detection by using deep autoencoders, IEEE/CAA J. Autom. Sin. 6 (2019) 441–451. https://doi.org/10.1109/JAS.2019.1911393.

[38] K. Wu, E. Otoo, K. Suzuki, Optimizing two-pass connected-component labeling algorithms, Pattern Anal. Appl. 12 (2009) 117–135. https://doi.org/10.1007/s10044-008-0109-y.

[39] J. Liu, L. Xu, Y. Xie, T. Ma, J. Wang, Z. Tang, W. Gui, H. Yin, H. Jahanshahi, Toward Robust Fault Identification of Complex Industrial Processes Using Stacked Sparse-Denoising Autoencoder With Softmax Classifier, IEEE Trans. Cybern. 53 (2023) 428–442. https://doi.org/10.1109/TCYB.2021.3109618.

[40] W. Yu, C. Zhao, Robust monitoring and fault isolation of nonlinear industrial processes using denoising autoencoder and elastic net, IEEE Trans. Control Syst. Technol. 28 (2020) 1083–1091. https://doi.org/10.1109/TCST.2019.2897946.

[41] S. Tao, T. Zhang, J. Yang, X. Wang, W. Lu, Bearing fault diagnosis method based on stacked autoencoder and softmax regression, Chinese Control Conf. CCC 2015-Septe (2015) 6331–6335. https://doi.org/10.1109/ChiCC.2015.7260634.